

Topological Phase Diagrams of Bulk and Monolayer $\text{TiS}_{2-x}\text{Te}_x$

Zhiyong Zhu, Yingchun Cheng, and Udo Schwingenschlög^{*}

Physical Sciences and Engineering Division, KAUST, Thuwal 23955-6900, Kingdom of Saudi Arabia
(Received 16 May 2012; revised manuscript received 25 November 2012; published 12 February 2013)

With the use of *ab initio* calculations, the topological phase diagrams of bulk and monolayer $\text{TiS}_{2-x}\text{Te}_x$ are established. Whereas bulk $\text{TiS}_{2-x}\text{Te}_x$ shows two strong topological phases [1;(000)] and [1;(001)] for $0.44 < x < 0.56$ and $0.56 < x < 1$, respectively, the monolayer is topologically nontrivial for $0.48 < x < 0.80$. Because in the latter doping range the topologically nontrivial nature survives down to a monolayer, $\text{TiS}_{2-x}\text{Te}_x$ is a unique system for studying topological phases in three and two dimensions simultaneously.

DOI: [10.1103/PhysRevLett.110.077202](https://doi.org/10.1103/PhysRevLett.110.077202)

PACS numbers: 75.70.Tj, 71.70.Ej, 73.22.-f, 85.75.-d

By the combination of spin-orbit interaction and time-reversal symmetry, the electronic band structures of topological insulators are topologically distinct. Therefore, they cannot be connected adiabatically to conventional insulators [1–6]. Gapless states with fascinating transport properties are guaranteed at the boundaries of such materials, where the topological invariants change. Two-dimensional topological insulators [7,8], also called quantum spin-Hall insulators, support spin-filtered edge states that exhibit dissipationless spin and charge transport, immune to nonmagnetic scattering [9]. In three dimensions [10–17], the spin-textured surface state is insensitive to atomic disorder and there is no backscattering between states of opposite momentum and spin due to quasiparticle interference [18,19]. In addition, exotic states can be induced by breaking various symmetries at the boundary. While the topological magnetoelectric effect results from broken time-reversal symmetry in an external magnetic field [1] or proximity to a magnetic material [20,21], topological superconductivity can be induced by breaking the gauge symmetry by proximity to a superconductor [22]. All these properties lead to a great potential of topological insulators in spintronics applications and quantum information processing [23]. The search for new materials remains a field of intensive research. Several families of two- [7,24–27] and three-dimensional [1,14,15,28–40] topological insulators have been proposed theoretically and, in part, have been confirmed experimentally [8–13,16–18].

In this Letter, we study the topological properties of $\text{TiS}_{2-x}\text{Te}_x$ in both bulk and monolayer form using all-electron *ab initio* calculations. We establish the topological phase diagrams and show that in a certain doping range a topologically nontrivial state is realized in both systems.

The transition-metal dichalcogenides TiS_2 and TiTe_2 are both layered compounds crystallizing in the $1T\text{-CdI}_2$ prototype structure with space group $P\bar{3}m1$ (No. 164) [41]. The Ti and S/Te atoms occupy $1a$ [(0,0,0)] and $2d$ [(1/3, 2/3, z)] Wyckoff sites, respectively; see Fig. 1(a). The crystal is composed of slabs weakly bound by van der Waals forces. In each slab, the Ti atoms are sandwiched

by S/Te atoms in an octahedral coordination via strong ionic-covalent bonding. The layered structure enables easy intercalation (removal) of impurity atoms into (from) the void between the layers. Therefore, TiS_2 is used in numerous applications, e.g., as cathode material in rechargeable batteries [42], as hydrogen storage material [43], and as a high-performance thermoelectric material [44]. The quasi-two-dimensional nature also enables the synthesis of various kinds of nanostructures, including stable monolayers as obtained by micromechanical cleavage and liquid exfoliation [45,46].

The following results have been obtained by full-potential linearized augmented plane wave calculations using the WIEN2K package [47]. A threshold energy of -6.0 Ry is used to separate the valence from core states. The same values of the muffin-tin radius $R_{\text{mt}} = 2.2$ bohr, plane wave cutoff $R_{\text{mt}}K_{\text{max}} = 10$, and highest orbital momentum $\ell_{\text{max}} = 10$ are used in all calculations, while $20 \times 20 \times 10$ and $20 \times 20 \times 2$ \vec{k} meshes are employed in the bulk and monolayer calculations, respectively. The electron exchange-correlation interaction is treated by a combination of the modified Becke-Johnson exchange potential and the local density approximation of the correlation potential (mBJLDA). This approach has demonstrated the ability to predict the band gap and band order with the same accuracy as computationally expensive hybrid functional and *GW* calculations for various types of compounds [48]. To confirm the validity of the mBJLDA approach for TiS_2 and TiTe_2 , we have conducted a comparative study

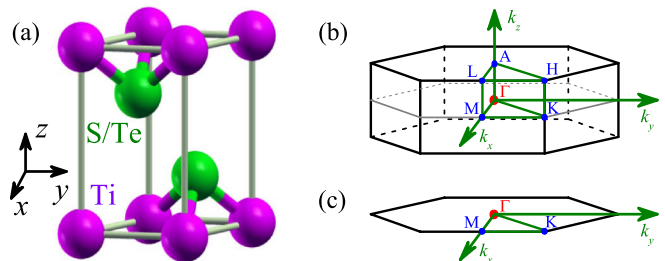


FIG. 1 (color online). (a) Unit cell of TiS_2 and TiTe_2 . First Brillouin zone of (b) bulk and (c) monolayer $\text{TiS}_{2-x}\text{Te}_x$.

using the generalized gradient approximation (GGA) and GW calculations. Whereas the GGA gives rise to a clearly too small band gap of 0.40 eV for TiS_2 , similar results of 0.73 and 0.78 eV are obtained by mBJLDA and GW calculations, respectively. In addition, the mBJLDA and GW calculations are found to result in the same band order, at both the Γ and A points. On the other hand, the band order is predicted incorrectly in our GGA calculations. Because of the agreement between the mBJLDA and GW calculations, the mBJLDA approach is confirmed to yield reliable results for both TiS_2 and TiTe_2 . Spin-orbit coupling is included in all calculations using a second-variational method with scalar relativistic orbitals as basis functions, where states up to 10 Ry above the Fermi energy (E_F) are included in the expansion. Lattice relaxations are performed applying the generalized gradient approximation [49] of the exchange-correlation potential in the absence of spin-orbit coupling. Forces are converged to less than 0.1 mRy/bohr.

In the calculations for the bulk materials, the experimental lattice constants [41] are adopted for TiS_2 ($a = 3.407 \text{ \AA}$, $c = 5.695 \text{ \AA}$) and TiTe_2 ($a = 3.777 \text{ \AA}$, $c = 6.498 \text{ \AA}$). The z values obtained by lattice relaxation for TiS_2 (0.2492) and TiTe_2 (0.2623) are close to the experimental values [41] of 0.2501 for TiS_2 and 0.2628 for TiTe_2 . For the monolayer systems, both a and the layer thickness d are optimized, yielding $a = 3.430 \text{ \AA}$, $d = 2.841 \text{ \AA}$ for TiS_2 and $a = 3.776 \text{ \AA}$, $d = 3.469 \text{ \AA}$ for TiTe_2 . In both cases, the reduction of the thickness down to the monolayer causes modifications of the bond lengths of less than 1%. This fact indicates a negligible effect of the interlayer van der Waals interaction on the structural properties, which has also been observed in the layered compounds MX_2 ($M = \text{Mo}, \text{W}$ and $X = \text{S}, \text{Se}$) [50].

Electronic band structures of bulk TiS_2 and TiTe_2 in the presence of spin-orbit coupling are shown in Figs. 2(a) and 2(b), respectively. In both materials, the S/Te p dominated valence states are close to fully occupied, whereas the Ti d dominated conduction states remain almost empty. This indicates a charge transfer from Ti to S/Te and reflects the ionic nature of the intralayer S/Te-Ti bonds. The states near E_F are composed of three S/Te p and three Ti d bands, which show at the Γ/A point odd ($2\Gamma_4^-/A_4^-$ and $1\Gamma_{56}^-/A_{56}^-$) and even parity ($2\Gamma_4^+/A_4^+$ and $1\Gamma_{56}^+/A_{56}^+$), respectively; see Figs. 2(c) and 2(d). In TiS_2 E_F separates the three odd parity from the three even parity states. Consequently, TiS_2 shows a semiconducting nature with an indirect band gap (valence band maximum at the Γ and conduction band minimum at the L point). In TiTe_2 the smaller electronegativity of Te as compared to that of S leads to a weaker p - d hybridization and a smaller energy separation between the p and d bands. Consequently, these bands are entangled around the Γ/A point near E_F , and the band gap is lost. Importantly, as compared to TiS_2 the band hierarchy is drastically modified in TiTe_2 . At the Γ point,

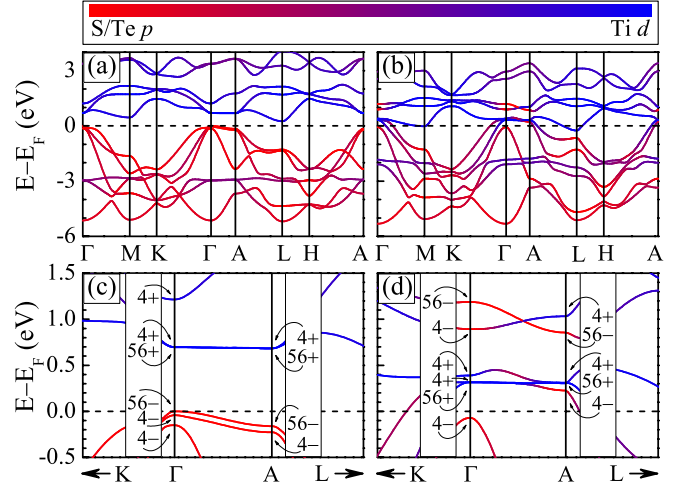


FIG. 2 (color online). Electronic band structures of bulk (a) TiS_2 and (b) TiTe_2 , in the presence of spin-orbit coupling. The S/Te p and Ti d band characters are indicated by different colors. Band hierarchy at the Γ and A points around E_F in bulk (c) TiS_2 and (d) TiTe_2 . The symmetry at the Γ/A point is labeled, and even/odd parity is indicated by $+/-$.

two of the three odd parity states ($1\Gamma_4^-$ and $1\Gamma_{56}^-$) are shifted above the three even parity states, while at the A point one of the three odd parity states ($1A_{56}^-$) now appears above two of the three even parity states ($1A_{56}^+$ and $1A_4^+$).

In three dimensions, the band topology is given by the four \mathbb{Z}_2 topological invariants ν_k with $k = 0, 1, 2, 3$. Whereas $\nu_{1,2,3}$ (the so-called weak topological invariants) are not robust against disorder, ν_0 is more fundamental and characterizes the strong topological insulator. The existence of inversion symmetry in bulk TiS_2 and TiTe_2 [see Fig. 1(a)] simplifies the calculation of ν_k . According to Ref. [1], it can be directly obtained from knowledge about the parity of each pair of occupied Kramers degenerate states at the eight time-reversal momenta (1Γ , $3M$, $1A$, and $3L$). In TiS_2 the products δ_i of the parities up to E_F are identical for all eight time-reversal momenta, yielding $\nu_{0,1,2,3} = 0$, i.e., a topologically trivial state [0;(000)]. For TiTe_2 , however, the situation is more complicated due to the switching of bands with different parity. As an even number of odd parity states is shifted above the even parity states at the Γ point, the sign of δ_Γ does not change. On the other hand, according to the above discussion the sign of δ_A changes. In addition, the other six δ_i remain the same due to the absence of band switching. Consequently, a topologically nontrivial state with \mathbb{Z}_2 class [1;(001)] is identified for TiTe_2 .

By gradually substitution of Te for S in TiS_2 , the discussed changes in the band order at the Γ and A points can occur one by one. Consequently, a complex topological phase diagram is expected for the ternary compound $\text{TiS}_{2-x}\text{Te}_x$ ($0 < x < 1$). Because the relative positions of the odd and even parity states at the M and L points are the same for bulk TiS_2 and TiTe_2 [see Figs. 2(a) and 2(b)], the

signs of δ_M and δ_L will not change when x varies from 0 to 1. Therefore, the values of ν_k are determined solely by δ_Γ and δ_A . Specifically, δ_Γ is determined by the energy differences Δ_Γ^1 between Γ_{56}^- and Γ_4^+ and Δ_Γ^2 between Γ_4^- and Γ_{56}^+ . Moreover, δ_A is determined by the energy differences Δ_A^1 between A_{56}^- and A_4^+ and Δ_A^2 between A_4^- and A_{56}^+ . Because TiS_2 and TiTe_2 have the same crystal structure except for the lattice parameters, no structural phase transition is expected to occur in $\text{TiS}_{2-x}\text{Te}_x$ as a function of x . In the following, we study the x dependence of δ_Γ and δ_A to obtain the topological phase diagram of bulk $\text{TiS}_{2-x}\text{Te}_x$, assuming a linear x dependence of Δ_Γ^1 , Δ_Γ^2 , Δ_A^1 , and Δ_A^2 .

For $x = 0$ (TiS_2) and $x = 1$ (TiTe_2), Δ_Γ^1 , Δ_Γ^2 , Δ_A^1 , and Δ_A^2 can be obtained from the electronic band structures in Fig. 2, resulting in the linear curves shown Fig. 3(a). Δ_Γ^1 and Δ_Γ^2 change their signs from negative to positive at $x = 0.44$ and $x = 0.56$, respectively. Furthermore, Δ_A^1 changes its sign from negative to positive at $x = 0.56$, while Δ_A^2 remains negative in the entire doping range. Therefore, as compared to TiS_2 , the signs of δ_Γ and δ_A change in the ranges $0.44 < x < 0.56$ and $0.56 < x < 1$, respectively. Calculation of the four \mathbb{Z}_2 invariants ν_k then leads to Fig. 3(a). Being topologically trivial [0;(000)] for $x < 0.44$, bulk $\text{TiS}_{2-x}\text{Te}_x$ shows two strong topological phases for $0.44 < x < 0.56$ [1;(000)] and $0.56 < x < 1$ [1;(001)]. It should be noted that the topologically nontrivial phases are actually semimetallic or metallic for the following reason: Because of the indirect nature of the band gap in TiS_2 [see Fig. 2(a)], the band switching at the Γ/A point as a function of x should occur above E_F with the lowest conduction band simultaneously shifted below E_F at the Γ/M point [see Fig. 2(b) for $x = 1$, for instance]. Accordingly, the topologically protected surface states of bulk $\text{TiS}_{2-x}\text{Te}_x$ lie above E_F and not exactly at E_F as in the prototypical topological insulator Bi_2Se_3 [14], for example. However, it is still possible to shift them to E_F by electron doping.

Two-dimensional topological insulators are not only of fundamental interest but also of technological significance

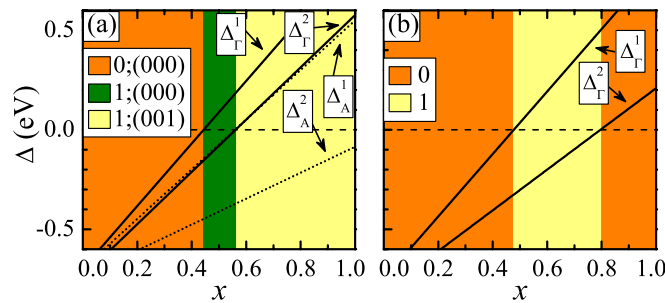


FIG. 3 (color online). (a) Topological phase diagram of bulk $\text{TiS}_{2-x}\text{Te}_x$ as a function of x , given by the energy differences between Γ_{56}^-/Γ_4^- and Γ_4^+/Γ_{56}^+ ($\Delta_\Gamma^1/\Delta_\Gamma^2$, solid lines) and between A_{56}^-/A_4^- and A_4^+/A_{56}^+ (Δ_A^1/Δ_A^2 , dotted lines). Different topological phases are indicated by different colors. (b) Topological phase diagram of monolayer $\text{TiS}_{2-x}\text{Te}_x$ as a function of x .

in nanoscale devices. When a three-dimensional topological insulator is thinned down toward the two-dimensional limit, the coupling between the two gapless boundary states on opposite surfaces can be strong enough for a finite gap to be opened [51]. The resultant gapped system can be either topologically trivial or nontrivial, depending on its thickness and the specific material [52–56]. In the following, we study the topological properties of monolayer $\text{TiS}_{2-x}\text{Te}_x$. We will show that the topologically nontrivial nature of the bulk compound survives in the monolayer for a certain range of x . This is of particular interest, because in all previously reported systems, such as Bi_2Se_3 and Bi_2Te_3 [52–56], the topologically nontrivial nature observed in three dimensions disappears in the two-dimensional limit. Because of quantum confinement, a monolayer has no band dispersion along k_z . Since there are four time-reversal momenta (1Γ and $3M$) in two dimensions, the topological nature is fully described by the single \mathbb{Z}_2 invariant ν . The invariant can be derived from the parities of the pairs of occupied Kramers degenerate states at the four time-reversal momenta [1].

In Figs. 4(a) and 4(b) we show the electronic band structures of monolayer TiS_2 and TiTe_2 , respectively, in the presence of spin-orbit coupling. Whereas TiS_2 is an indirect band gap semiconductor, TiTe_2 turns out to be semimetallic. The valence band maximum is located at the Γ point and the conduction band minimum at the M point, in both materials. Similar to the bulk, the states at the Γ point near E_F comprise three p and d bands with odd ($2\Gamma_4^-$ and $1\Gamma_{56}^-$) and even ($2\Gamma_4^+$ and $1\Gamma_{56}^+$) parity, respectively. In TiS_2 , E_F separates the three odd parity states from the three even parity states and a topologically trivial nature ($\nu = 0$) is established. In TiTe_2 , two of the three odd parity states

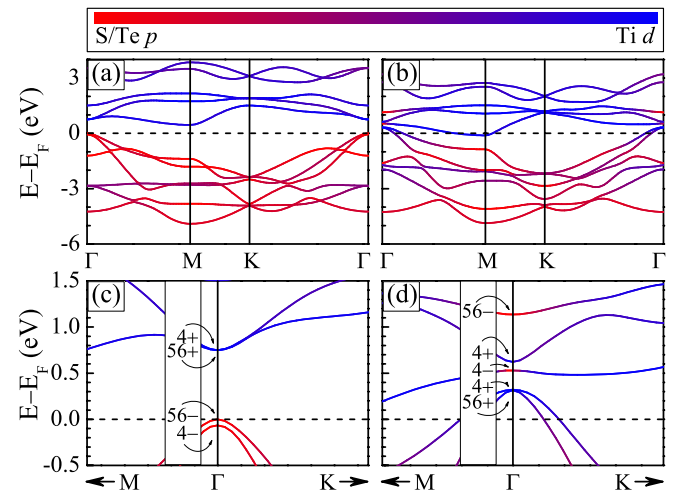


FIG. 4 (color online). Electronic band structures of monolayer (a) TiS_2 and (b) TiTe_2 , in the presence of spin-orbit coupling. The S/Te p and Ti d band characters are indicated by different colors. Band hierarchy at the Γ and A points around E_F in bulk (c) TiS_2 and (d) TiTe_2 . The symmetry at the Γ/A point is labeled, and even/odd parity is indicated by $+/-$.

($1\Gamma_4^-$ and $1\Gamma_{56}^-$) are shifted above two of the three even parity states ($1\Gamma_4^+$ and $1\Gamma_{56}^+$), while no band switching is observed at the M point. As a consequence, δ_Γ does not change and TiTe_2 is also topologically trivial ($\nu = 0$). Because of the band switching at the Γ point, we expect topological phase transitions as a function of x . Following the same procedure used for the bulk materials, the topological phase diagram of monolayer $\text{TiS}_{2-x}\text{Te}_x$ is obtained; see Fig. 3(b). A topologically nontrivial state appears at $x = 0.48$ ($\nu = 1$) and vanishes at $x = 0.80$. Similar to the case in bulk $\text{TiS}_{2-x}\text{Te}_x$, the topologically protected edge states lie above E_F but can be shifted to E_F by electron doping.

The complex topological phase diagrams of bulk and monolayer $\text{TiS}_{2-x}\text{Te}_x$ are a consequence of the small energy separation between the p -like valence and d -like conduction bands around the Γ and A points and the high sensitivity of the band hierarchy to x . In addition, the role of spin-orbit coupling is critical. First, it ensures a doping range in which the material is topologically nontrivial. Analysis shows that the two odd parity states that participate in the band switching ($1\Gamma_{56}^-/A_{56}^-$ and $1\Gamma_4^-/A_4^-$) have p_{xy} character. Without the spin-orbit coupling they would be degenerate; see (I) in Fig. 5(a). However, a finite energy difference between the two p_{xy} states (Δ_Γ/Δ_A) is a prerequisite of the topologically nontrivial phase because otherwise an even number of odd parity states would be shifted above the even parity states simultaneously at the Γ and A points. Second, the spin-orbit coupling influences Δ_Γ/Δ_A and, hence, indirectly the x range of the topologically nontrivial phase. Without spin-orbit coupling, the p_{xy} and p_z states would have doublet Γ_3^-/A_3^- and singlet Γ_2^-/A_2^- symmetries at Γ/A ; see (I) in Fig. 5(a). The inclusion of spin-orbit coupling yields a hybridization of the p_{xy} and p_z Γ_4^-/A_4^- states; see (II) in Fig. 5(a). Therefore, Δ_Γ/Δ_A is determined not only by the strength of the spin-orbit coupling but also by the strength of this hybridization, which is given by the energy difference Δ'_Γ/Δ'_A between the two states; see (III) in Fig. 5(a). This relationship between Δ_Γ/Δ_A and Δ'_Γ/Δ'_A is reflected by the data in Fig. 5(b).

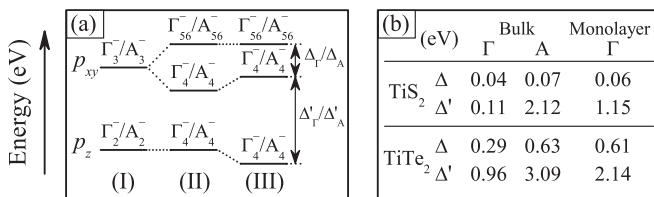


FIG. 5. (a) Energy diagram of the p_{xy} and p_z states at the Γ/A point near E_F in $\text{TiS}_2/\text{TiTe}_2$ (I) without spin-orbit coupling, (II) with spin-orbit coupling but without hybridization between the two Γ/A_4^- states, and (III) with spin-orbit coupling and hybridization. (b) Energy differences Δ_Γ/Δ_A between the p_{xy} Γ/A_{56}^- and Γ/A_4^- states and Δ'_Γ/Δ'_A between the p_{xy} and p_z Γ/A_4^- states for bulk and monolayer TiS_2 and TiTe_2 .

In conclusion, all-electron *ab initio* calculations have been used to study the band topology of bulk and monolayer $\text{TiS}_{2-x}\text{Te}_x$. The topological phase diagram has been established for both morphologies by an analysis of the band switching at the Γ and A points near E_F . For bulk $\text{TiS}_{2-x}\text{Te}_x$, two strong topological phases [1;(000)] and [1;(001)] have been identified for the doping ranges $0.44 < x < 0.56$ and $0.56 < x < 1$, respectively. Moreover, monolayer $\text{TiS}_{2-x}\text{Te}_x$ turns out to be topologically nontrivial for $0.48 < x < 0.80$. Therefore, the topologically nontrivial nature of bulk $\text{TiS}_{2-x}\text{Te}_x$ survives in this doping range when the thickness is reduced to a monolayer. This is a novel property, because usually a topologically nontrivial nature vanishes in the two-dimensional limit [52–56]. Ternary $\text{TiS}_{2-x}\text{Te}_x$ thus is unique in the sense that it hosts both two- and three-dimensional topological phases.

*Corresponding author.

udo.schwingschlogl@kaust.edu.sa

- [1] L. Fu and C. L. Kane, *Phys. Rev. B* **76**, 045302 (2007).
- [2] L. Fu, C. L. Kane, and E. J. Mele, *Phys. Rev. Lett.* **98**, 106803 (2007).
- [3] J. E. Moore and L. Balents, *Phys. Rev. B* **75**, 121306 (2007).
- [4] R. Roy, *Phys. Rev. B* **79**, 195322 (2009).
- [5] M. Z. Hasan and C. L. Kane, *Rev. Mod. Phys.* **82**, 3045 (2010).
- [6] X.-L. Qi and S.-C. Zhang, *Rev. Mod. Phys.* **83**, 1057 (2011).
- [7] B. A. Bernevig, T. L. Hughes, and S.-C. Zhang, *Science* **314**, 1757 (2006).
- [8] M. König, S. Wiedmann, C. Brüne, A. Roth, H. Buhmann, L. W. Molenkamp, X.-L. Qi, and S.-C. Zhang, *Science* **318**, 766 (2007).
- [9] A. Roth, C. Brüne, H. Buhmann, L. W. Molenkamp, J. Maciejko, X.-L. Qi, and S.-C. Zhang, *Science* **325**, 294 (2009).
- [10] D. Hsieh, D. Qian, L. Wray, Y. Xia, Y. S. Hor, R. J. Cava, and M. Z. Hasan, *Nature (London)* **452**, 970 (2008).
- [11] D. Hsieh, Y. Xia, D. Qian, L. Wray, J. H. Dil, F. Meier, J. Osterwalder, L. Patthey, J. G. Checkelsky, N. P. Ong, A. V. Fedorov, H. Lin, A. Bansil, D. Grauer, Y. S. Hor, R. J. Cava, and M. Z. Hasan, *Nature (London)* **460**, 1101 (2009).
- [12] Y. L. Chen, J. G. Analytis, J.-H. Chu, Z. K. Liu, S.-K. Mo, X. L. Qi, H. J. Zhang, D. H. Lu, X. Dai, Z. Fang, S. C. Zhang, I. R. Fisher, Z. Hussain, and Z. X. Shen, *Science* **325**, 178 (2009).
- [13] Y. Xia, D. Qian, D. Hsieh, L. Wray, A. Pal, H. Lin, A. Bansil, D. Grauer, Y. S. Hor, R. J. Cava, and M. Z. Hasan, *Nat. Phys.* **5**, 398 (2009).
- [14] H. Zhang, C.-X. Liu, X.-L. Qi, X. Dai, Z. Fang, and S.-C. Zhang, *Nat. Phys.* **5**, 438 (2009).
- [15] H.-J. Zhang, C.-X. Liu, X.-L. Qi, X.-Y. Deng, X. Dai, S.-C. Zhang, and Z. Fang, *Phys. Rev. B* **80**, 085307 (2009).
- [16] T. Sato, K. Segawa, H. Guo, K. Sugawara, S. Souma, T. Takahashi, and Y. Ando, *Phys. Rev. Lett.* **105**, 136802 (2010).

- [17] Y.L. Chen, Z.K. Liu, J.G. Analytis, J.-H. Chu, H.J. Zhang, B.H. Yan, S.-K. Mo, R.G. Moore, D.H. Lu, I.R. Fisher, S.C. Zhang, Z. Hussain, and Z.X. Shen, *Phys. Rev. Lett.* **105**, 266401 (2010).
- [18] D. Hsieh, Y. Xia, L. Wray, D. Qian, A. Pal, J.H. Dil, J. Osterwalder, F. Meier, G. Bihlmayer, C.L. Kane, Y.S. Hor, R.J. Cava, and M.Z. Hasan, *Science* **323**, 919 (2009).
- [19] P. Roushan, J. Seo, C.V. Parker, Y.S. Hor, D. Hsieh, D. Qian, A. Richardella, M.Z. Hasan, R.J. Cava, and A. Yazdani, *Nature (London)* **460**, 1106 (2009).
- [20] X.-L. Qi, T.L. Hughes, and S.-C. Zhang, *Phys. Rev. B* **78**, 195424 (2008).
- [21] A.M. Essin, J.E. Moore, and D. Vanderbilt, *Phys. Rev. Lett.* **102**, 146805 (2009).
- [22] L. Fu and C.L. Kane, *Phys. Rev. Lett.* **100**, 096407 (2008).
- [23] C. Nayak, S.H. Simon, A. Stern, M. Freedman, and S. Das Sarma, *Rev. Mod. Phys.* **80**, 1083 (2008).
- [24] C.L. Kane and E.J. Mele, *Phys. Rev. Lett.* **95**, 226801 (2005).
- [25] S. Murakami, *Phys. Rev. Lett.* **97**, 236805 (2006).
- [26] C. Liu, T.L. Hughes, X.-L. Qi, K. Wang, and S.-C. Zhang, *Phys. Rev. Lett.* **100**, 236601 (2008).
- [27] C.-C. Liu, W. Feng, and Y. Yao, *Phys. Rev. Lett.* **107**, 076802 (2011).
- [28] A. Shitade, H. Katsura, J. Kuneš, X.-L. Qi, S.-C. Zhang, and N. Nagaosa, *Phys. Rev. Lett.* **102**, 256403 (2009).
- [29] S. Chadov, X. Qi, J. Kuebler, G.H. Fecher, C. Felser, and S.C. Zhang, *Nat. Mater.* **9**, 541 (2010).
- [30] H. Lin, L.A. Wray, Y. Xia, S. Xu, S. Jia, R.J. Cava, A. Bansil, and M.Z. Hasan, *Nat. Mater.* **9**, 546 (2010).
- [31] M. Dzero, K. Sun, V. Galitski, and P. Coleman, *Phys. Rev. Lett.* **104**, 106408 (2010).
- [32] D. Xiao, Y. Yao, W. Feng, J. Wen, W. Zhu, X.-Q. Chen, G.M. Stocks, and Z. Zhang, *Phys. Rev. Lett.* **105**, 096404 (2010).
- [33] B. Yan, C.-X. Liu, H.-J. Zhang, C.-Y. Yam, X.-L. Qi, T. Frauenheim, and S.-C. Zhang, *Europhys. Lett.* **90**, 37002 (2010).
- [34] W. Feng, D. Xiao, J. Ding, and Y. Yao, *Phys. Rev. Lett.* **106**, 016402 (2011).
- [35] H. Jin, J.-H. Song, A.J. Freeman, and M.G. Kanatzidis, *Phys. Rev. B* **83**, 041202 (2011).
- [36] S.V. Eremeev, G. Bihlmayer, M. Vergniory, Y.M. Koroteev, T.V. Menshchikova, J. Henk, A. Ernst, and E.V. Chulkov, *Phys. Rev. B* **83**, 205129 (2011).
- [37] L.-L. Wang and D.D. Johnson, *Phys. Rev. B* **83**, 241309 (2011).
- [38] B. Sa, J. Zhou, Z. Song, Z. Sun, and R. Ahuja, *Phys. Rev. B* **84**, 085130 (2011).
- [39] Y. Sun, X.-Q. Chen, C. Franchini, D. Li, S. Yunoki, Y. Li, and Z. Fang, *Phys. Rev. B* **84**, 165127 (2011).
- [40] Z.Y. Zhu, Y.C. Cheng, and U. Schwingenschlögl (unpublished).
- [41] Y. Arnaud and M. Chevreton, *J. Solid State Chem.* **39**, 230 (1981).
- [42] M.S. Whittingham, *Chem. Rev.* **104**, 4271 (2004).
- [43] J. Chen, S.-L. Li, Z.-L. Tao, Y.-T. Shen, and C.-X. Cui, *J. Am. Chem. Soc.* **125**, 5284 (2003).
- [44] C.L. Wan, Y.F. Wang, N. Wang, W. Norimatsu, M. Kusunoki, and K. Koumoto, *J. Electron. Mater.* **40**, 1271 (2011).
- [45] C. Lee, H. Yan, L.E. Brus, T.F. Heinz, J. Hone, and S. Ryu, *ACS Nano* **4**, 2695 (2010).
- [46] J.N. Coleman *et al.*, *Science* **331**, 568 (2011).
- [47] P. Blaha, K. Schwarz, G.K.H. Madsen, D. Kvasnicka, and L. Luitz, *WIEN2K, an augmented plane wave plus local orbitals program for calculating crystal properties* (TU Vienna, Vienna, 2001).
- [48] F. Tran and P. Blaha, *Phys. Rev. Lett.* **102**, 226401 (2009).
- [49] J.P. Perdew, K. Burke, and M. Ernzerhof, *Phys. Rev. Lett.* **77**, 3865 (1996).
- [50] Z.Y. Zhu, Y.C. Cheng, and U. Schwingenschlögl, *Phys. Rev. B* **84**, 153402 (2011).
- [51] H.-Z. Lu, W.-Y. Shan, W. Yao, Q. Niu, and S.-Q. Shen, *Phys. Rev. B* **81**, 115407 (2010).
- [52] Y. Zhang, K. He, C.-Z. Chang, C.-L. Song, L.-L. Wang, X. Chen, J.-F. Jia, Z. Fang, X. Dai, W.-Y. Shan, S.-Q. Shen, Q. Niu, X.-L. Qi, S.-C. Zhang, X.-C. Ma, and Q.-K. Xue, *Nat. Phys.* **6**, 584 (2010).
- [53] Y.-Y. Li, G. Wang, X.-G. Zhu, M.-H. Liu, C. Ye, X. Chen, Y.-Y. Wang, K. He, L.-L. Wang, X.-C. Ma, H.-J. Zhang, X. Dai, Z. Fang, X.-C. Xie, Y. Liu, X.-L. Qi, J.-F. Jia, S.-C. Zhang, and Q.-K. Xue, *Adv. Mater.* **22**, 4002 (2010).
- [54] J. Linder, T. Yokoyama, and A. Sudbø, *Phys. Rev. B* **80**, 205401 (2009).
- [55] C.-X. Liu, H. Zhang, B. Yan, X.-L. Qi, T. Frauenheim, X. Dai, Z. Fang, and S.-C. Zhang, *Phys. Rev. B* **81**, 041307 (2010).
- [56] M. Liu, C.-Z. Chang, Z. Zhang, Y. Zhang, W. Ruan, K. He, L.-L. Wang, X. Chen, J.-F. Jia, S.-C. Zhang, Q.-K. Xue, X.-C. Ma, and Y.-Y. Wang, *Phys. Rev. B* **83**, 165440 (2011).